IEEE Open Journal of Antennas and Propagation

Received XX Month XXXX; revised X Month XXXX; accepted XX Month XXXX. Date of publication XX Month XXXX; date of current version XX Month XXXX.

Digital Object Identifier 10.1109/OAJPE.2020.2976889

Highly-Integrated Dual-Polarized Multibeam MM-Wave Array Antenna With Ultra-High Tx-Rx Isolation for In-Band Full Duplex (IBFD) Application

Tong Wu[1], Fanchao Zeng[2], Graduate Student MEMBER, IEEE, Xiaodong Yang[1], Senior MEMBER, IEEE, Weisen Guo[1] AND Zhiya Zhang[1], MEMBER, IEEE

[1]National Key Laboratory of Radar Detection and Sensing, Xidian University, Xi'an 710071, China
[2]Global Big Data Technologies Center, University of Technology Sydney (UTS), Sydney, NSW 2007, Australia

CORRESPONDING AUTHOR: Zhiya Zhang (e-mail: zyzhang@xidian.edu.cn); Fanchao Zeng(e-mail: Fanchao.Zeng@student.uts.edu.au)

This work is supported by the National Natural Science Foundation of China under General Program 62271372.

ABSTRACT This article analyzes the current development status and requirements of wireless communication technology, and proposes a multibeam MM-wave antenna array with high-isolation for in-band full duplex (IBFD) wireless integrated access and backhaul application based on this analysis. A bistatic simultaneous transmitting and receiving antenna architecture, a low loss multibeam antenna array architecture based on Rotman lenses, and an antenna packaging design based on multi-layer PCB technology are comprehensively applied in the antenna design. For the isolation design of the transmitting and receiving antennas, this article innovatively adopts a defective ground and a novel uneven choke baffle loaded on curved surfaces, which improves the in-band isolation of the transmitting and receiving antennas by at least 20dB. Finally, a prototype was fabricated, capable of generating three beams for both the Tx and Rx arrays, with an isolation exceeding 80 dB across all Tx and Rx beams. The antenna prototype has been applied to the testing of 5G wireless duplex IAB system.

INDEX TERMS In-Band Full Duplex (IBFD), Multibeam antenna, MM-wave, Ultra-high TX-RX isolation, Uneven choke baffle, Defected ground, Rotman Lens, 5/6G

I. INTRODUCTION

In recent years, the explosive growth of mobile communication data traffic has become an undeniable fact. According to the prediction of the International Telecommunication Union (ITU), the mobile communication volume in 2030 is expected to be 80 times that of 2020, mainly carried by cellular networks [1]. The growth of communication capacity requires data rates of several tens of Gbps [2]. Therefore, an efficient and robust backhaul technology is essential in the face of the surge in future data interactions. Especially wireless integrated access and backhaul (IAB) technology based on 5G network is considered a highly competitive solution that can replace fiber optics [1]. A potential implementation of wireless IAB scenario is depicted in Fig. 1, which includes IAB-donor, IAB access unit (IAB-AU), IAB mobile terminal (IAB-MT). For the requirement of higher channel capacity and transmission rate, the full duplex IAB mechanism is essential in this application.

However, most existing IAB systems still operate under time-division duplex (TDD) or frequency-division duplex (FDD) schemes, which are inherently half-duplex in nature. Although these techniques enable alternating or simultaneous transmission and reception, they rely on separating the two in either time or frequency, resulting in inefficient spectrum utilization [1]. Achieving truly in-band full-duplex (IBFD) operation requires an antenna system capable of simultaneously transmitting and receiving over the same frequency band with high transmit–receive (TR) isolation—a critical technical challenge.

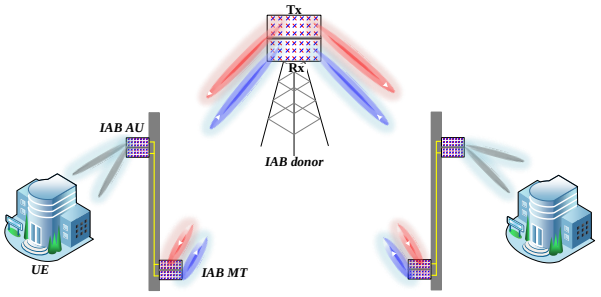

FIGURE 1. A potential implementation of IAB scenario based on full duplex transceiver array antenna

In recent years, research on IBFD antennas has yielded promising results [3]. Specifically, monostatic IBFD antennas typically achieve TR isolation through near-field cancellation or by employing carefully designed feeding networks and the

parasitic structures [4]–[8]. Meanwhile, bistatic IBFD antennas rely on techniques such as spatial separation, high-impedance surfaces (HIS), metal baffles, absorbers, and near-field cancellation to suppress mutual coupling between the transmitting and receiving paths [9]–[13]. These strategies have proven effective for improving isolation in various IBFD configurations.

Nonetheless, existing IBFD antennas are mostly designed as single-beam or omnidirectional systems [14]–[18]. These configurations suffer from low gain and limited spatial control, making them unsuitable for long-range millimeter-wave (mm-wave) IAB applications. With mm-wave expected to play a central role in future wireless communication systems [19], the need for directional, high-gain, and flexible beamforming antennas is increasingly urgent. Although some efforts, such as [20], have explored beam-scanning IBFD arrays using conventional phased-array architectures, these designs tend to incur high power consumption and cost, and they fall short of the energy efficiency and scalability goals envisioned for beyond 5G (B5G) and 6G networks. Furthermore, the monostatic configuration in [20] limits TR isolation to merely 32 dB, far below the levels required for robust IBFD operation.

Multibeam antenna technology offers significant advantages for full-duplex IAB applications. By supporting simultaneous communication across multiple spatial directions, multibeam systems enhance spectral efficiency, enable concurrent access and backhaul links, and allow dynamic resource allocation without mechanical movement. This capability is especially valuable in mm-wave environments with high user density and relay diversity. However, integrating multibeam capability into an IBFD system greatly increases design complexity. In such systems, mutual coupling must be suppressed not only between individual transmitting and receiving elements, but across multiple beam paths. Achieving high TR isolation under these conditions requires advanced feeding and packaging schemes, as well as novel decoupling strategies. Thus, the successful realization of a multibeam IBFD antenna represents a critical step toward enabling practical, high-capacity full-duplex IAB systems.

Furthermore, many existing IBFD antenna designs overly emphasize compactness and miniaturization, often at the cost of insufficient spatial isolation—a key factor in maximizing TR isolation performance [17]. For instance, while [21] achieves over 70 dB of TR isolation, it does so using orthogonally polarized transmitting and receiving antennas, which inherently differ in radiation characteristics and thus do not constitute a true IBFD system. Similarly, [22] adopts a back-to-back configuration that leverages pattern isolation but results in entirely different radiation patterns for transmission and reception, again falling short of the IBFD standard. Even the widely cited work in [9] achieves its isolation (over 60 dB) through large spatial separation and HIS loading, which are difficult to implement in compact systems. To address these limitations, it is essential to reconsider spatial resource utilization in IBFD antenna design. This is particularly feasible in IAB donor nodes, where antenna installation is typically fixed and only IAB-AU and IAB-MT require limited mobility. Moreover, at mm-wave and even terahertz frequencies, the physical size of antennas becomes sufficiently small, enabling more sophisticated spatial arrangements without compromising form factor. As such, exploring spatial and structural strategies for improving TR isolation is key to advancing full-duplex IAB deployment.

In summary, despite notable advancements in IBFD antenna technologies, there remains a gap in targeted research for full-duplex IAB applications in B5G/6G environments. Existing solutions often lack support for energy-efficient multibeam operation, suffer from limited TR isolation, or fail to leverage the spatial flexibility afforded by mm-wave implementations. These challenges call for a novel antenna architecture that integrates high-gain multibeam design, efficient packaging, and robust isolation measures into a compact and scalable IBFD platform.

In response to the challenges outlined above, this paper proposes a novel bistatic multibeam IBFD antenna array tailored for full-duplex IAB systems. The main innovations and contributions of this work are summarized as follows:

First, to the best of the authors' knowledge, this is the first reported multibeam in-band full-duplex (IBFD) antenna design. A Rotman lens is employed to feed a mm-wave microstrip antenna array, enabling high gain and beam-steering capability while avoiding the excessive power consumption and cost associated with conventional phased array systems. To achieve a compact and energy-efficient architecture, the Rotman lens, power-dividing network, and antenna elements are fully integrated using Antenna-in-Package (AiP) technology. This integration minimizes interconnection distances, effectively reducing insertion loss and supporting the green design objectives of future wireless systems. Second, leveraging the bistatic architecture, this paper introduces—for the first time—a defected ground plane (DGP) as a spatial decoupling strategy. By engineering the ground structure, the antenna's radiation pattern is reshaped to reduce field intensity along the dominant coupling path, thereby mitigating mutual coupling at its source. Third, to further suppress residual coupling—particularly that caused by edge diffraction in traditional metal baffle structures—a novel uneven choke baffle with curved surface loading is proposed. The specially shaped surface reduces diffraction at the baffle edges, thereby improving isolation from spatially coupled waves. Additionally, by optimizing the slot depth between baffles, the structure effectively attenuates both surface waves and space waves, further enhancing isolation.

Measurement results verify the effectiveness of the proposed design. The fabricated prototype demonstrates excellent impedance matching and beam-switching performance across the 26–26.8 GHz frequency range. Remarkably, the measured in-band isolation exceeds 92 dB at its peak and maintains a minimum of 68 dB across all beams. To the best of the authors' knowledge, this represents the highest isolation level achieved among AIP-based multibeam IBFD antennas in the FR2 band to date. The prototype has also been applied in a full-duplex 5G IAB test system, resulting in a cell throughput gain of approximately 84% compared to a conventional TDD-based deployment [1].

The remainder of this paper is organized as follows: Section II describes the architecture and packaging of the transmitting

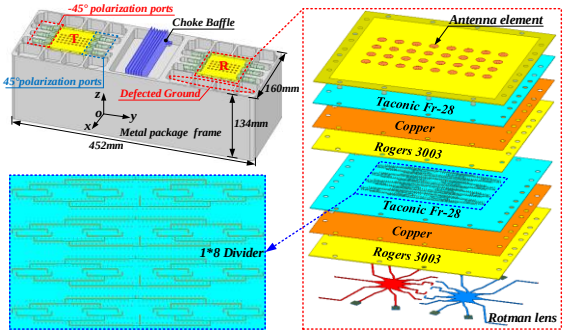

FIGURE 2. **The architecture of the transceiver antenna array**

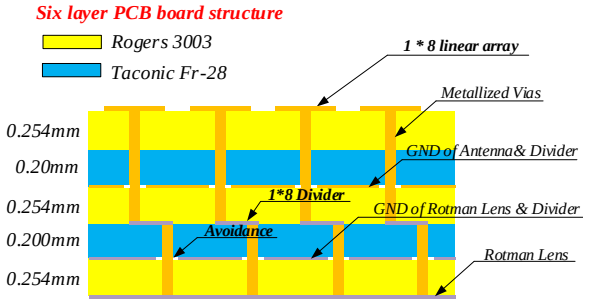

FIGURE 3. **The package layout of the antenna array**

and receiving antenna arrays. Section III details the design and simulation of the Rotman lens. Section IV presents the design of the antenna elements, power divider, and multilayer PCB integration. The TR isolation strategy, including the defected ground and choke baffle structures, is discussed in Section V. Section VI outlines the fabrication and experimental validation of the prototype, and Section VII concludes the paper.

II. ARCHITECTURE AND PACKAGING OF ANTENNAS

The overall structure of the antenna is shown in the Fig. 2. The antenna is integrated by AIP technology based on multilayer PCB for first stage integration; The antennas, decoupling measures and digital logic circuit which hidden in a metal packaging frame for beam switching control are second integrated onto the packaging frame. This IBFD antenna array adopts a bistatic form, the transmitting and receiving antenna arrays are placed separately, thereby achieving high spectrum utilization while providing sufficient space for high isolation design. The high isolation module based on a choke baffle is loaded in the middle of the transmitting and receiving antenna arrays. The antenna arrays operating in the 5G FR2 frequency band. Due to the relatively high frequency band, the bistatic transceiver antenna array and isolation modules can still maintain the compactness of the overall structure after being packaged as a whole.

For the consideration of environment-friendly, a Rotman lens is used to achieve multibeam of the antenna, which avoids the energy consumption of a large number of active devices in traditional phased array antennas. This article also considers factors such as ensuring diversity reception of the antenna system, improving anti-interference capabilities and increasing capacity, the antenna is designed with a ±45° dual line polarization. Therefore, each antenna array is equipped

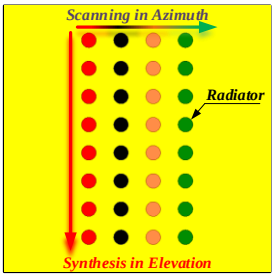

FIGURE 4. **Synthesis and scanning of the antenna array**

with two Rotman lenses. As shown in Fig. 2, the feeding ports for different polarizations are located on both sides of the antenna. To further reduce the interconnection loss between the beam scanning network and the antenna, and to achieve a compact design, the antenna element adopts a circular microstrip form, and realize the integrated of the Rotman lens, feeding network and radiator through AIP technology.

The specific antenna package layout is shown in the Fig. 3, a six-layer PCB is designed through three layers of Rogers3003 core substrate and two layers of Taconic Fr-28 prepreg. The Rotman lens is printed on the bottom of the underlying PCB, its output ports are separately connected to the feeding network, a 1*8 divider, through the metallized via hole from the avoidance hole. The output ports of divider are connected to antenna elements through the metallized via hole to realize the feed. The divider feeds the 1*8 elements in the elevation dimension of the antenna as shown in Fig. 4. Four such power dividers are connected to the output ports of the Rotman lens respectively, so that realize the beam switching of 4*8 scale antenna array in the azimuth dimension.

III. ROTMAN LENS

In the design of Rotman lens, the principle of equal optical path is used to obtain the electrical constraints of the lens contour, the geometric constraints are obtained by the coordinate relationship between the lens focus and the beam port contour, thereby solving the lens contour. Key design parameters that need to be considered include the maximum scanning angle β, focal angle α, the number of beams and output ports, focal length F and focal length ratio g, the dielectric material used, the overall size of the lens, and all optimization parameters that determine the aperture phase error.

Among these parameters, the β is set to 16° here, and the number of beams is 3 with 4 output ports, achieving beam switching of -16°, 0°, and 16°. The α is generally the same as the β. This Rotman lens only has three beam ports, which correspond to three focus, so there is no need to consider the optimization of aperture phase error. Therefore, F and g can be appropriately selected based on factors such as lens size optimization and installation space limitations. Finally, in the process of the lens design, F and g were selected as 1.05 and 7.5mm respectively, and the simulation model of the lens shown in the Fig. 5 is obtained. The substrate is Rogers RO3003, ($\varepsilon r = 3$, and $\tan\delta = 0.0013$), thickness is 0.254mm. In order to reduce mutual coupling and phase error between lens ports, four dummy ports were set in this model.

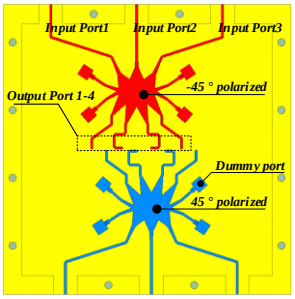

FIGURE 5. Simulation model of the Rotman lens

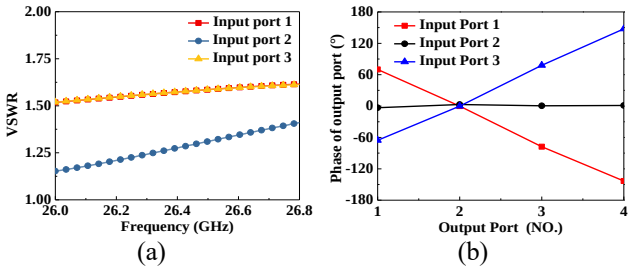

FIGURE 6. (a)VSWR and (b) Phase of output during operation of different input ports.

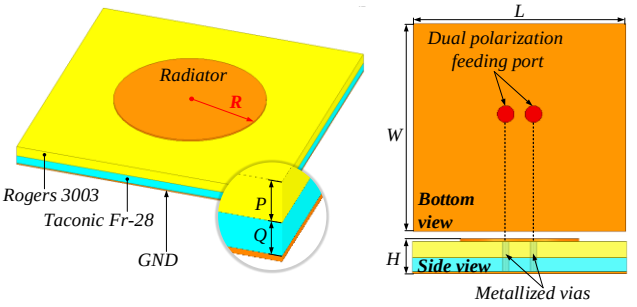

FIGURE 7. Structure of the antenna element

TABLE 1. Deviation between output port phase and ideal phase

Phase (°)	Output Port1	Output Port2	Output Port3	Output Port4
Input Port 1	0.4	0	-8.2	4.3
Input Port 2	-3.1	3.0	3.2	-3.1
Input Port 3	4.1	0.0	-8.5	8.7

TABLE 2. Insertion loss of each input port

Input Port	1	2	3
Insertion Loss (dB)	2.2	1.7	2.2

As shown in Fig. 5, the two lenses for ±45° polarization are completely centrally symmetrical, the -45° polarized lens is used as an example to illustrate the performance of the lens. The VSWRs of input ports 1-3 are shown in Fig.6(a), which are all below 1.6. The output phases of the Rotman lens are shown as Fig.6(b).

Since β is set to 16° and the azimuth dimension element spacing is 8mm, the ideal phase gradient is 69.5°. The output phase deviation of each port compared with the ideal phase is shown in Table 1, and the maximum phase deviation is 8.7°. The insertion loss of each input port is shown in Table 2. The insertion loss deviation among ports is 0.5dB.

TABLE 3. Dimensions of the antenna element

L	W	H	R	P	Q
8mm	7mm	0.524mm	1.815mm	0.254mm	0.2mm

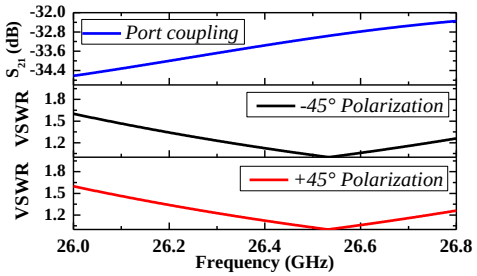

FIGURE 8. Port parameters of the antenna element

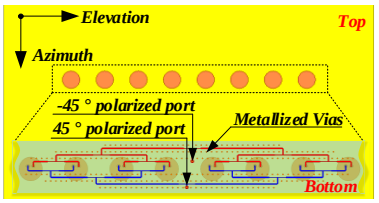

FIGURE 9. Model of power divider and 1 × 8 linear array

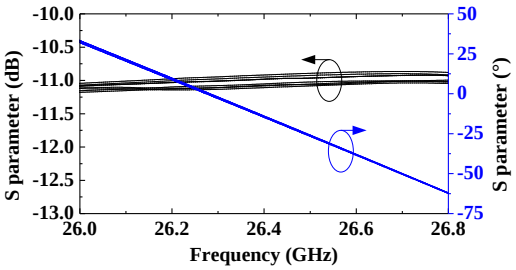

FIGURE 10. S-parameter from input to output ports of 1×8 power divider

IV. ANTENNA ELEMENT AND ARRAY DESIGN

When using multi-layer PCB technology for AIP design, prepregs need to be pressed between the dielectric substrate to achieve adhesion, so dielectric substrate and prepregs are placed alternately, and the two together form the substrate, as shown in Fig. 7, of the antenna. The dielectric film is Rogers3003 (ε_r =3, and tanδ=0.0013), thickness is 0.254mm. The prepreg is Taconic Fr-28(ε_r=2.74, and tanδ=0.0017), thickness is 0.2mm. The specific structure of the antenna element is shown in Fig. 7. The structure of the element is simple and easy to integrate, so it can reduce processing errors, which is crucial for mm-wave antennas. The optimized sizes of the antenna elements are shown in Table 3. The dual polarization port parameters of the antenna element are shown in Fig. 8.

As can be seen from Fig. 9, the antenna elements first form a one-dimensional linear array fed by 1*8 power divider. Each linear array has two such power divider for ±45°polarization feeding separately. In addition, in order to reduce internal electromagnetic leakage and network insertion loss, metalized via holes with shielding effect are installed around the divider. According to Fig. 10, the insertion loss of the power divider is lower than 2dB. The amplitude of different output ports of the

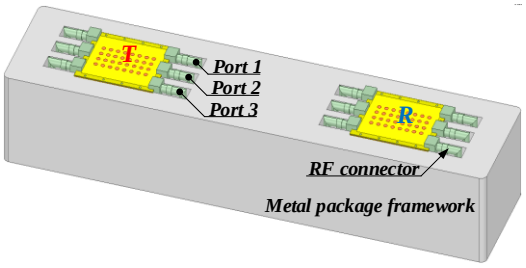

FIGURE 11. Schematic diagram of transceiver array antenna without isolation measures loaded

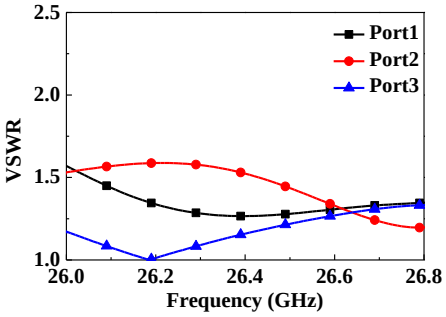

FIGURE 12. VSWR of transceiver array antenna

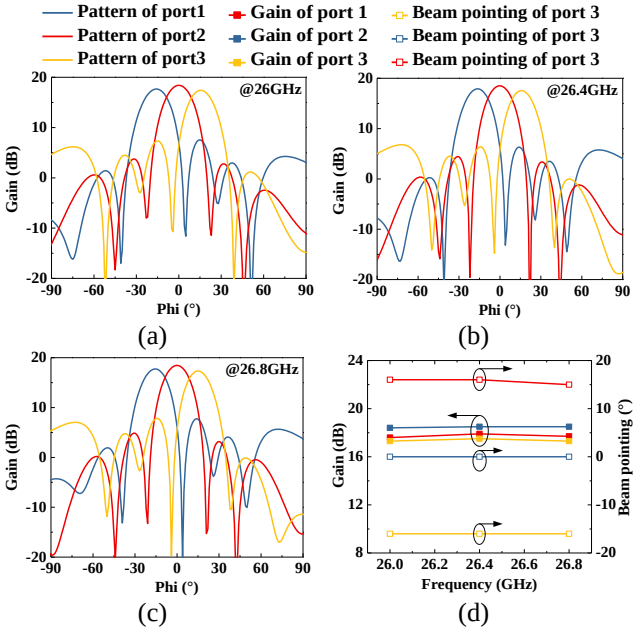

FIGURE 13. Simulated patterns at (a)26GHz, (b) 26.4GHz, (c)26.8GHz and (d)corresponding gain and beam pointing

power divider is high consistency, and the phase is also the same. Therefore, this power divider can achieve the excellent effect of equal power division.

After completing the design of each component of the array, the AIP is realized through the multi-layer PCB architecture shown in Fig. 2 and Fig. 3. As a result, a 4*8 antenna array integrating the radiator, feeding network, and Rotman lens can be obtained as shown in the Fig. 11. The control module for beam switching of the antenna array is hidden inside the metal frame, and will not be elaborated as part of the antenna here. Furthermore, the transmitting and receiving antenna arrays are

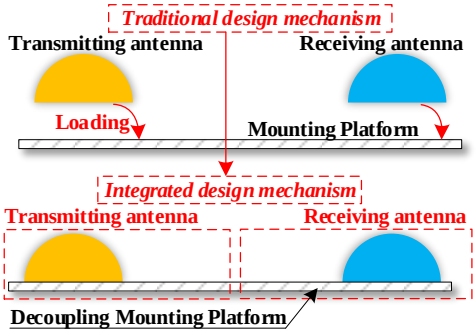

FIGURE 14. Integrated Design Mechanism of Bistatic IBFD Antenna and Isolation Measures

placed separately on a metal packaging frame to achieve the subsequent bistatic high isolation design. Taking the feeding ports of -45° polarization shown in Fig.11 as example, their VSWRs are all lower than 1.6 as shown in Fig. 12. The radiation patterns at 26GHz, 26.4GHz and 26.8GHz of the antenna array are shown in Fig. 13(a), (b), (c). The corresponding gain are shown in Fig. 13(d), which can reach 18dB, and the beam pointing does not deviate greatly from the theoretical value. These results show that beam scanning can be achieved well without pattern distortion.

V. DESIGNS FOR ULTRA-HIGH ISOLATION

Based on the coupling mechanism between the transmitting and receiving antennas, the coupling modes are mainly classified into spatial wave coupling and surface wave coupling. Therefore, this paper applies targeted decoupling measures to simultaneously suppress both spatial and surface coupling waves, achieving a universal method for the ultra - high isolation design of bistatic IBFD antennas. The specific design is as follows.

A. Defected Ground Design

As shown in Fig. 14, for bistatic IBFD antennas, in the traditional transmit-receive isolation design, the antennas passively adapt to the mounting platform. The antennas, mounting platform, and isolation measures are independent of each other, resulting in limited decoupling effects and being unfavorable for the integration. To address this issue, this paper innovatively proposes an integrated design method for the mounting platform-antenna-isolation measures. By integrating the isolation measures and the mounting platform into the antenna design, the decoupling problem of the antennas is transformed into the design of the antenna radiation pattern. This reduces the radiation intensity along the coupling path between the transmitting and receiving antennas, thereby enhancing the isolation.

Specifically, when the transmitting antenna is installed on a smooth and flat metal ground, its radiated waves will easily excite surface waves. The surface waves propagate laterally along the boundary between the ground and air, resulting in a significant coupling between the transmitting and receiving antenna. Therefore, based on this coupling mechanism and the proposed design method, this paper designs a DGP structure for mounting ground of the antenna, enabling it to function as a part of the antenna to suppress the lateral radiation waves.

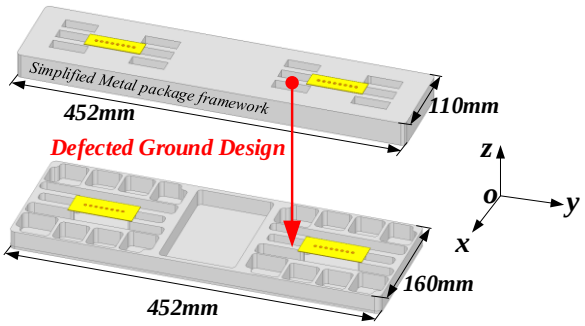

FIGURE 15. Defect ground structure and simplified simulation model for isolation

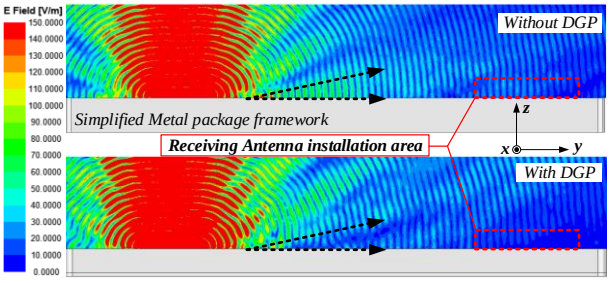

FIGURE 16. Distribution of transmitting E-field in airspace above metal platform

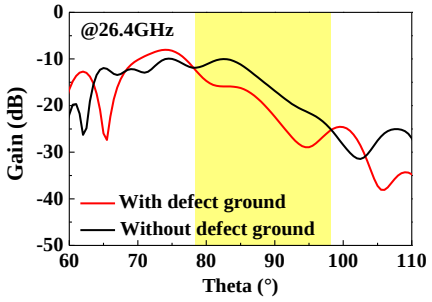

FIGURE 17. Lateral pattern at YOZ plane of the transmitting antenna array before and after loading the defect ground

As shown in Fig. 15, this article designs the defected ground structure in the form of a grid metal beam. The motivation for adopting this structural shape are as follows: First, to minimize the transmission path of surface currents; second, to ensure the structural strength as much as possible while implementing the defective ground design, thereby guaranteeing the stability of the antenna installation; third, to avoid a significant increase in the weight of the platform. Regarding the determination of its dimensions, the optimization is guided by the reduction of the antenna's lateral radiation intensity. By comparing the simulation results of the antenna's lateral radiation intensity under different sizes and corresponding numbers of defective squares, and considering the degree of deterioration of the platform's weight, a reasonable choice can be made. In the middle of the metal platform is a large concave flat structure, which is designed to facilitate the loading of structures that enhancing the isolation in subsequent designs.

Furthermore, as shown in Fig. 15, when conducting simulation analysis on the isolation between the transmitting and receiving antenna, we simplified the simulation model by

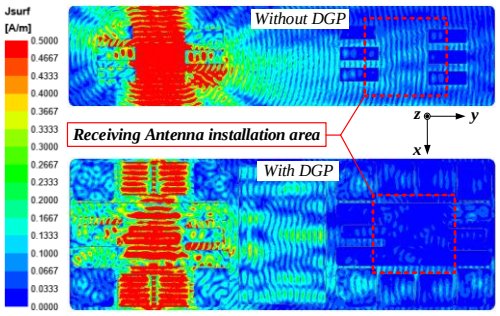

FIGURE 18. Comparison of the surface current of the normal ground and the defect ground plane(DGP)

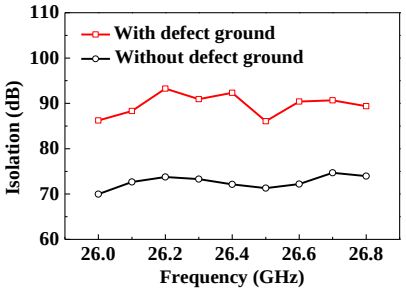

FIGURE 19. Isolation improvement after the loading of defect ground

only retaining the antenna installation area of the metal packaging platform, and using a one-dimensional linear array as the transmitting and receiving antenna, thereby reducing the computational resource occupation of the antenna simulation and highlighting the analysis of the effect of isolation measures. This simplified design of the model not only improves the simulation accuracy of transmission and reception isolation, but also greatly improving the simulation efficiency.

The E-field distribution above the metal packaging platform during the operation of the transmitting antenna array before and after loading the defect ground structure at 26.4GHz is shown in Fig. 16. Obviously, when the transmitting antenna array is installed on a smooth floor without defects, the E-field strength in the black dashed line angle space in Fig. 16 is significantly higher than that loading the defect ground. Especially for the installation area of the receiving antenna array, the E-field strength decreases significantly after loading the defect ground. The lateral directional pattern of YOZ plane of the transmitting antenna array before and after loading the defect ground is shown in Fig. 17. Within the spatial range of 78.5°-98°, the maximum E-field strength after loading the defect ground can be reduced by 7.8dB, with an average reduction of 5.1dB. The analysis of the above changes in E-field strength indicates that defect ground can effectively suppress the coupled surface waves excited by the transmitting antenna.

In fact, due to the suppression of surface waves, the surface current excited by the transmitting antenna array also decreases accordingly. As shown in Fig. 18, the red dashed rectangle represents the loading area of the receiving array, where the surface current intensity at 26.4GHz shows a significant decrease after loading the defective structure.

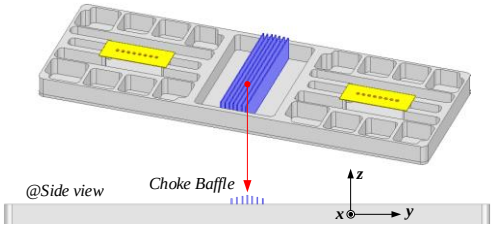

FIGURE 20. Schematic diagram of choke baffle loading

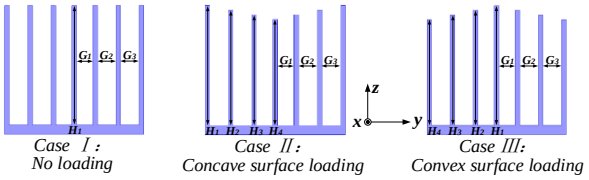

FIGURE 21. Surface loading of the choke baffle

Therefore, the defective structure of the ground has a significant suppression effect on both coupled surface waves and coupled surface currents. Finally, as shown in Fig. 19, under the effect of the defect ground, the isolation increases by an average of 17dB in the band of 26-26.8GHz.

B. A Novel Uneven Choke Baffle Design

From the above simulation, it can be seen that there is still a certain degree of coupling current on the floor after loading the defected ground, and the spatial radiation waves of the transmitting array can also cause coupling of the transceiver antennas. Therefore, on the basis of the defected ground, this article also for the first time proposed a novel uneven choke baffle, which can obviously improve the isolation.

Due to the zero tangential component of the electric field on the metal surface, TE surface waves cannot be transmitted in the metal plane. However, for TM surface waves, additional loading measures are required to suppress them, such as choke. The surface impedance of the choke can be calculated by this equation:

$$Z_s = jZ_0 \tan kd$$

$Z_0 = 377\Omega$ is the inherent impedance of air or free space, d is the ripple depth, and k is the phase constant. Based on this, when the depth d is taken as $\lambda/4+(\lambda/2) * n$ (n=1, 2, 3...), Z_s tends to infinity, resulting in high impedance to the surface current. The depth d of a conventional choke is generally taken as $\lambda/4$ of its operating frequency. This article appropriately selects the value of the n to increase the height of the metal plate of the choke, so that it not only serves as a choke, but also as a metal baffle to reflect spatially coupled waves. Therefore, the choke baffle proposed here have both the decoupling function of choke and metal baffle.

As shown in Fig. 20, from the perspective of suppressing spatial coupling waves, a higher choke baffle, a better decoupling effect. However, in order to ensure the miniaturization of the system, facilitate installation, and minimize the impact of the baffle on antenna performance, the baffle should not be too high.

Due to the fact that the relative operating bandwidth of the antenna is only 3.03%, the height of the baffle can be selected according to the wavelength λ of center frequency 26.4GHz

TABLE 4. Dimensions of the choke baffle

G1	G2	G3	H1	H2	H3	H4
4mm	4mm	3.5mm	28mm	27mm	26mm	25mm

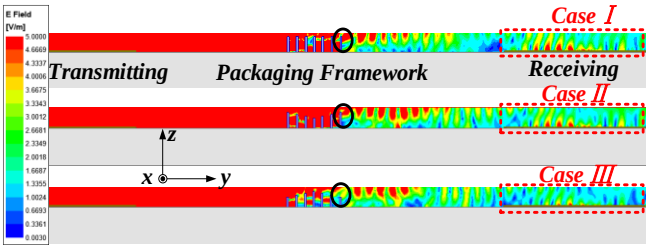

FIGURE 22. Electric field distribution of the antenna after different curved surface loadings of the choke baffle

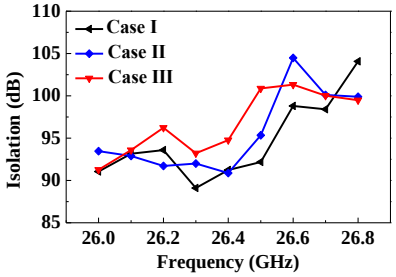

FIGURE 23. Decoupling effect of choke baffle under different surface loading

The λ of 26.4GHz is 11.36mm, so the height of the baffle is selected as $\lambda/4+(\lambda/2) * 4$=25.57mm. From Fig. 20, it can be seen that this height is higher than the antenna aperture, which can effectively block the lateral radiation space waves of the antenna and ensure the miniaturization of the platform.

Because of the choke baffle is composed of metal, diffraction is inevitable when suppressing spatially coupled waves, leading to the emergence of new coupling paths. Therefore, concave and convex surface is loaded as shown in the Fig. 21 to suppress the diffraction. As shown in Fig. 21, there are seven baffles in total, forming six choke slots. The baffles and slots are symmetrical. During the process of surface loading on the choke baffle, we optimize the height and slot width of the choke baffle to maximize the decoupling effect. The specific dimensions are shown in Table 4.

As shown in Fig. 22, the left side is the transmitting antenna, the right side is the receiving antenna, and the choke baffle is in the middle. Obviously, after the choke baffle is loaded, the transmitting electric field at 26.4GHz on the left side can be significantly suppressed during the process of propagating to the receiving antenna on the right side. From the area circled by the black solid line, it can be seen that although the traditional metal baffle effectively blocks spatial coupled waves, its all-metal structure causes strong diffraction at the right edge, which generates secondary coupling and weakens the isolation performance of the metal baffle. By contrast, after applying curved surface loading—especially convex curved surface loading—to the metal baffle, the diffraction at the right edge is effectively reduced. Therefore，as shown in the area circled by the red dashed, the electric field excited on the receiving antenna by the transmitting electric field is minim in case III.

Furthermore, as shown in Fig. 23, the isolation between the

TABLE 5. Average isolation in case I-III

Case	I	II	III
Average isolation(dB)	94.63	95.64	96.75

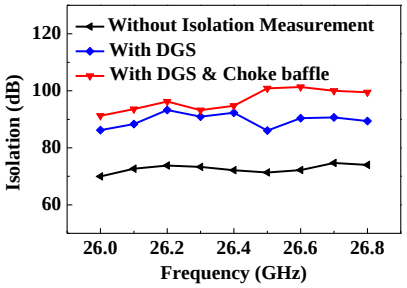

FIGURE 24. Decoupling effect under different measures

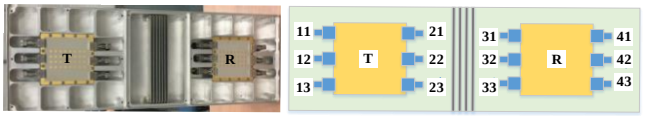

(a) (b)

FIGURE 25. (a)Antenna prototype and (b) its ports number

transmitting and receiving antenna arrays increased after the loading of the choke baffle. As shown in Table 5, compared to the case without surface loading, the average isolation increased from 94.63dB to 95.64dB after loading with the concave surface, and reached 96.75dB when loading with the convex surface. And the in-band fluctuation of the isolation is smaller when loading convex surfaces. Therefore, in the subsequent prototype processing, a convex curved surface is loaded on the choke baffle.

Finally, as shown in Fig. 24, by the loading of these measures, the isolation of the transceiver array can be increased from 72.67dB to 96.75dB in average. Obviously, the defective structure and the novel choke baffle can significantly achieve the purpose of decoupling.

VI. FABRICATION AND MEASUREMENT

To validate the proposed design, the antenna array was fabricated, the prototype is shown in the Fig. 25(a). For ease of expression, ports of the antenna are numbered in the order shown in Fig. 25(b). Ports 11-13 and 31-33 indicates the -45° polarization port, ports 21-23 and 41-43 indicates the 45° polarization port. The "T" represents transmitting antenna array, and the "R" represents the receiving antenna array. Taking the transmitting antenna ports of -45° polarization as example, the measured patterns are shown in Fig. 26. It can be seen from Fig. 26(a)-(c) that the prototype can achieve beam switching ± 16° well. The measured gain and beam pointing of each port are shown in Fig.26 (d). Overall, the switching beam gain drop at each measured frequency point is lower than 1.8dB.

Due to the high TR isolation, the received signal level of the receiving antenna array is low. In order to ensure the measurement accuracy, the measurement of the TR isolation is carried out in an anechoic chamber environment. A spectrum analyzer is used to observe the received signal, and

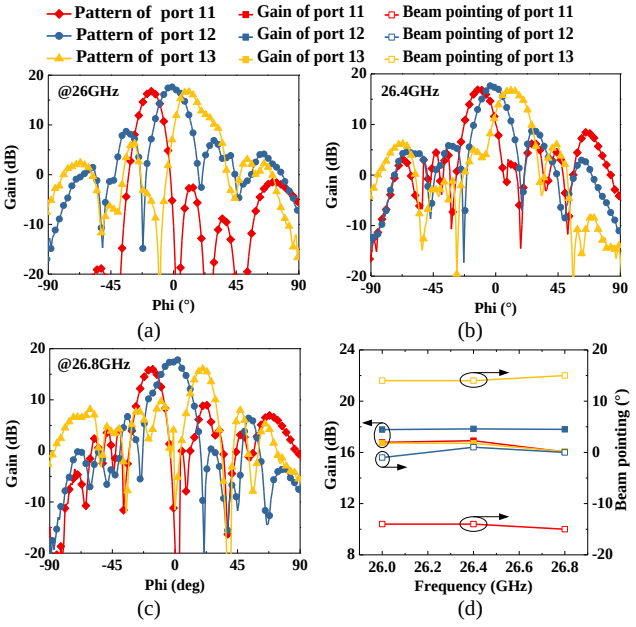

FIGURE 26. (a)Measured patterns at (a)26GHz, (b) 26.4GHz, (c)26.8GHz and (d)corresponding gain and beam pointing

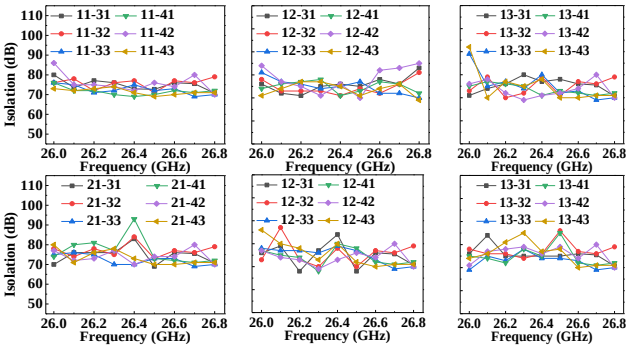

FIGURE 27. Measured isolation between different transmission and reception ports

its noise floor is adjusted to be lower than -120 dBm.

The measured isolation between different transmission and reception ports are shown in the Fig. 27. Obviously, the isolation is not less than 68dB, the maximum can reach over 92dB, and the average can reach over 75dB. This shows that through the proposed decoupling measures, a high isolation between the transmitting and receiving antennas can be effectively realized. For IBFD antenna, this isolation level is relatively high in current research findings. It should be pointed out that there is a deviation between the measured and the simulated isolation. This is partly due to the fact that the antenna in the simulation is a one-dimensional linear array model, while the measured antenna is a planar array. On the other hand, it is also due to the processing error of the antenna and the metal platform. Therefore, the deviation of the measured results does not affect the correctness of the simulation analysis mentioned earlier.

To further demonstrate the superiority of the antenna design scheme proposed in this paper, a performance comparison is conducted between the proposed IBFD antenna suitable for full-duplex IAB system and other IBFD antennas. The specific

TABLE 6. Performance comparison of proposed antenna with the reported references

Ref.	Polari-zation	Beam	Isolation(dB)	Gain (dB)	Integrated
[4]	single	single	＞50	20	No
[9]	dual	single	＞60	7	No
[15]	single	single	＞34	11.9	No
[17]	single	single	＞30	5	No
[18]	single	single	＞33	17.7	No
[20]	single	scanning	＞35	15	No
This work	dual	multibeam	＞68	18	Yes

comparison contents are shown in Table 6. Obviously, the transceiver antenna array proposed in this paper can simultaneously meet the performance requirements of polarization diversity, high integration, high TR isolation, green and low-power-consumption beam switching, and high gain, which can provide a more targeted IBFD antenna design scheme for full-duplex IAB.

VII. CONCLUSION

This article proposes a full duplex millimeter wave array antenna that combines high spectrum utilization, low power consumption, and integrated packaging characteristics to meet the application requirements of future wireless full duplex IAB. It adopts a bistatic IBFD architecture, and ultimately achieve a transmission and reception isolation of over 68dB through the design of defected ground and curved uneven surface choke baffles. The overall package size of the transceiver antenna array is 452mm × 160mm × 134mm, and it has used for 5G wireless backhaul system testing. Therefore, the proposed antenna and decoupling measures are good candidate for wireless full duplex IAB applications.

REFERENCES

[1] B. Yu *et al.*, "Realizing High Power Full Duplex in Millimeter Wave System: Design, Prototype and Results," *IEEE J. Sel. Areas Commun.*, vol. 41, no. 9, pp.82-89, Sep. 2023.

[2] B. Aqlan, M. Himdi, H. Vettikalladi, and L. Le-Coq, "A circularly polarized sub-terahertz antenna with low-profile and high-gain for 6G wireless communication systems," *IEEE Access*, vol. 9, pp. 122607-122617, Sep. 2021.

[3] K. E. Kolodziej, B. T. Perry and J. S. Herd, "In-Band Full-DuplexTechnology: Techniques and Systems Survey," *IEEE Trans. Microw. Theory Tech.*, vol. 67, no. 7, pp. 3025-3041, Jul. 2019.

[4] P. Valale Prasannakumar, M. A. Elmansouri, L. B. Boskovic, M. Ignatenko and D. S. Filipovic, "Wideband Quasi-Monostatic Simultaneous Transmit and Receive Reflector Antenna," *IEEE Trans. Antennas Propag.*, vol. 68, no. 4, pp. 2630-2637, Apr. 2020.

[5] E. A. Etellisi, M. A. Elmansouri and D. S. Filipović, "Wideband Multimode Monostatic Spiral Antenna STAR Subsystem," *IEEE Trans. Antennas Propag.*, vol. 65, no. 4, pp. 1845-1854, Apr. 2017.

[6] W. -G. Lim, W. -I. Son, K. S. Oh, W. -K. Kim and J. -W. Yu, "Compact Integrated Antenna With Circulator for UHF RFID System," *IEEE Antennas Wirel. Propag. Lett.*, vol. 7, pp. 673-675, Mar. 2008.

[7] D. Wu, Y. -X. Sun, R. Lian, B. Xiao, M. Li and K. -D. Xu, "Metasurface Antenna With Cocircularly Polarized Radiation Characteristics for Wideband Monostatic Simultaneous Transmit and Receive Applications," *IEEE Trans. Antennas Propag.*, vol. 71, no. 4, pp. 3304-3313, Apr. 2023.

[8] K. Y. Yang, W. J. Zhu, L. H. Ye, J. -F. Li and D. -L. Wu, "Metamaterial-Based Low-Profile Broadband In-Band Full-Duplex Antenna," *IEEE Antennas Wirel. Propag. Lett.*, vol. 22, no. 8, pp. 1942-1946, Aug. 2023.

[9] P. V. Prasannakumar, M. A. Elmansouri and D. S. Filipovic, "Wideband Decoupling Techniques for Dual-Polarized Bi-Static Simultaneous Transmit and Receive Antenna Subsystem," *IEEE Trans. Antennas Propag.*, vol. 65, no. 10, pp. 4991-5001, Oct. 2017.

[10] D. Wu et al., "Wideband Monostatic Co-Horizontally Polarized Simultaneous Transmit and Receive Antenna Subsystem With Integrated Beamforming Network," *IEEE Trans. Antennas Propag.*, vol. 70, no. 2, pp. 1505-1510, Feb. 2022.

[11] J. I. Choi, M. Jain, K. Srinivasan, P. Levis, and S. Katti, "Achieving single channel, full duplex wireless communication," in *Proceedings of the sixteenth annual international conference on Mobile computing and networking*, Chicago, USA, 2010, pp. 1-12.

[12] P. V. Prasannakumar, M. A. Elmansouri, and D. S. Filipovic, "Wideband decoupling techniques for dual-polarized bi-static simultaneous transmit and receive antenna subsystem," *IEEE Trans. Antennas Propag.*, vol. 65, no. 10, pp. 4991-5001, Oct. 2017.

[13] A. T. Wegener and W. J. Chappell, "High isolation in antenna arrays for simultaneous transmit and receive," in *2013 IEEE International Symposium on Phased Array Systems and Technology*, Boston, USA 2013, pp. 593-597.

[14] D. Wu, Y. Zang, H. Luyen, M. Li and N. Behdad, "A Compact, Low-Profile Simultaneous Transmit and Receive Antenna With Monopole-Like Radiation Characteristics," *IEEE Antennas Wirel. Propag. Lett.*, vol. 18, no. 4, pp. 611-615, Apr. 2019.

[15] A. Sharma et al., "In-Band RCS Reduction and Isolation Enhancement of a 24 GHz Radar Antenna Using Metamaterial Absorber for Sensing and Automotive Radar Applications," *IEEE Sensors Journal*, vol. 20, no. 21, pp. 13086-13093, 1 Nov. 2020.

[16] R. Lian, T. -Y. Shih, Y. Yin and N. Behdad, "A High-Isolation, Ultra-Wideband Simultaneous Transmit and Receive Antenna With Monopole-Like Radiation Characteristics," *IEEE Trans. Antennas Propag.*, vol. 66, no. 2, pp. 1002-1007, Feb. 2018.

[17] A. H. Abdelrahman and D. S. Filipovic, "Antenna System for Full-Duplex Operation of Handheld Radios," *IEEE Trans. Antennas Propag.*, vol. 67, no. 1, pp. 522-530, Jan. 2019.

[18] K. -R. Xiang, F. -C. Chen, Y. -Z. Liang, Q. Xue and Q. -X. Chu, "Co-Polarized In-Band Full-Duplex Cavity Slot Antenna Array Based on Wavefront Phase Compensation," *IEEE Trans. Antennas Propag.*, vol. 72, no. 8, pp. 6401-6411, Aug. 2024.

[19] W. Hong et al., "The Role of Millimeter-Wave Technologies in 5G/6G Wireless Communications," *IEEE Journal of Microw.*, vol. 1, no. 1, pp. 101-122, Jan. 2021.

[20] A. Hovsepian, E. A. Alwan and J. L. Volakis, "A Wideband, Scanning Array of Four-Arm Spiral Elements for Simultaneous Transmit and Receive," *IEEE Antennas Wirel. Propag. Lett.*, vol. 19, no. 4, pp. 537-541, Apr. 2020

[21] H. Nawaz and I. Tekin, "Dual-Polarized, Differential Fed Microstrip Patch Antennas With Very High Interport Isolation for Full-Duplex Communication," *IEEE Trans. Antennas Propag.*, vol. 65, no. 12, pp. 7355-7360, Dec. 2017.

[22] M. Heino, S. N. Venkatasubramanian, C. Icheln and K. Haneda, "Design of Wavetraps for Isolation Improvement in Compact In-Band Full-Duplex Relay Antennas," *IEEE Trans. Antennas Propag.*, vol. 64, no. 3, pp. 1061-1070, Mar. 2016.

[23] L. Chi, Z. Weng, Y. Qi and J. L. Drewniak, "A 60 GHz PCB Wideband Antenna-in-Package for 5G/6G Applications," *IEEE Antennas Wirel. Propag. Lett.*, vol. 19, no. 11, pp. 1968-1972, Nov. 2020

[24] K. -Q. Huang and M. Swaminathan, "Antenna Array on Glass Interposer for 6G Wireless Communications," *IEEE Trans. Compon., Packag. Manuf. Technol.*, vol. 13, no. 2, pp. 211-218, Feb. 2023

[25] X. Jia et al., "Antenna With Embedded Die in Glass Interposer for 6G Wireless Applications," *IEEE Trans. Compon., Packag. Manuf. Technol.*, vol. 13, no. 2, pp. 219-229, Feb. 2023